



# Additive Manufacturing: Metallurgy, Cut Analysis & Porosity

12 Advanced Optical Metrology

Additive Manufacturing: Metallurgy, Cut Analysis & Porosity

EVIDENT OLYMPUS

WILEY

The latest eBook from  
Advanced Optical Metrology.  
Download for free.

In industry, sector after sector is moving away from conventional production methods to additive manufacturing, a technology that has been recommended for substantial research investment.

Download the latest eBook to read about the applications, trends, opportunities, and challenges around this process, and how it has been adapted to different industrial sectors.

**EVIDENT**  
OLYMPUS

**WILEY**

# Direct and Label-Free Cell Status Monitoring of Spheroids and Microcarriers Using Microfluidic Impedance Cytometry

Lingyan Gong, Chayakorn Petchakup, Pujiang Shi, Pei Leng Tan, Lay Poh Tan, Chor Yong Tay, and Han Wei Hou\*

**3D cellular spheroids/microcarriers (100 μm–1 mm) are widely used in bio-manufacturing, and non-invasive biosensors are useful to monitor cell quality in bioprocesses. In this work, a novel microfluidic approach for label-free and continuous-flow monitoring of single spheroid/microcarrier (hydrogel and Cytodex) based on electrical impedance spectroscopy using co-planar Field's metal electrodes is reported. Through numerical simulation and experimental validation, two unique impedance signatures ( $|Z_{LF}|$  (60 kHz),  $|Z_{HF}|$  (1 MHz)) which are optimal for spheroid growth and viability monitoring are identified. Using a closed-loop recirculation system, it is demonstrated that  $|Z_{LF}|$  increases with breast cancer (MCF-7) spheroid biomass, while higher opacity (impedance ratio  $|Z_{HF}|/|Z_{LF}|$ ) indicates cell death due to compromised cell membrane. Anti-cancer drug (paclitaxel)-treated spheroids also exhibit lower  $|Z_{LF}|$  with increased cell dissociation. Interestingly, impedance characterization of adipose-derived mesenchymal stem cell differentiation on Cytodex microcarriers reveals that adipogenic cells (higher intracellular lipid content) exhibit higher impedance than osteogenic cells (more conductive due to calcium ions) for both microcarriers and single cell level. Taken together, the developed platform offers great versatility for multi-parametric analysis of spheroids/microcarriers at high throughput ( $\approx 1$  particle/s), and can be readily integrated into bioreactors for long-term and remote monitoring of biomass and cell quality.**

## 1. Introduction

3D cellular spheroids are self-organizing clusters of cells ( $\approx 100$  μm–1 mm in size) which show great promises in drug

cytotoxicity assessment due to close resemblance of intercellular and cell-matrix complexities *in vivo*.<sup>[1–3]</sup> Microcarriers are bead-based 3D matrix scaffolds ( $\approx 100$ –400 μm in diameter) used to upscale cell culture processes in tissue engineering<sup>[4,5]</sup> and cell therapies.<sup>[6,7]</sup> As these cultures may last from several days to months,<sup>[8]</sup> real-time monitoring of spheroid/microcarrier status in a label-free and non-invasive manner is of great significance in many bioprocesses. Conventional sensors for bioreactors probe changes in culture media properties (pH, dissolved oxygen, temperature etc.) that are affected by biomass. As quantification of cell metabolites in culture media indirectly indicates cell/spheroid growth, it is not suitable for real-time monitoring due to a delay between metabolites change and the cell state.<sup>[9]</sup>

Unlike single cells, an inherent problem for optical imaging of 3D spheroids/microcarriers is their large sizes which limit light penetration and fluorescent staining.<sup>[10]</sup> Typically, cellular aggregates are dissociated into single cells and stained to determine viability as

endpoint measurements.<sup>[11,12]</sup> Electrical impedance spectroscopy is a label-free approach for characterization of material dielectric properties in a static (non-flow) manner,<sup>[13]</sup> and has been recently applied in microfluidic systems to monitor 3D

L. Gong, Dr. C. Petchakup, Prof. H. W. Hou  
School of Mechanical and Aerospace Engineering  
Nanyang Technological University  
50 Nanyang Avenue, Singapore 639798  
E-mail: hwhou@ntu.edu.sg

Dr. P. Shi, P. L. Tan, Prof. L. P. Tan, Prof. C. Y. Tay  
School of Materials Science and Engineering  
Nanyang Technological University  
50 Nanyang Avenue, Singapore 639798

Prof. C. Y. Tay  
School of Biological Sciences  
Nanyang Technological University  
60 Nanyang Drive, Singapore 637551

The ORCID identification number(s) for the author(s) of this article can be found under <https://doi.org/10.1002/smll.202007500>.

DOI: 10.1002/smll.202007500

Prof. C. Y. Tay  
Environmental Chemistry and Materials Centre  
Nanyang Environment and Water Research Institute  
1 CleanTech Loop, CleanTech One, Singapore 637141

Prof. C. Y. Tay  
Energy Research Institute  
Nanyang Technological University Singapore  
50 Nanyang Drive, Singapore 637553

Prof. H. W. Hou  
Lee Kong Chian School of Medicine  
Nanyang Technological University  
11 Mandalay Road, Singapore 308232

Prof. H. W. Hou  
Critical Analytics for Manufacturing of Personalized Medicine  
Singapore-Massachusetts Institute of Technology Alliance for Research and Technology  
1 CREATE Way, #10-01, CREATE Tower, Singapore 138602

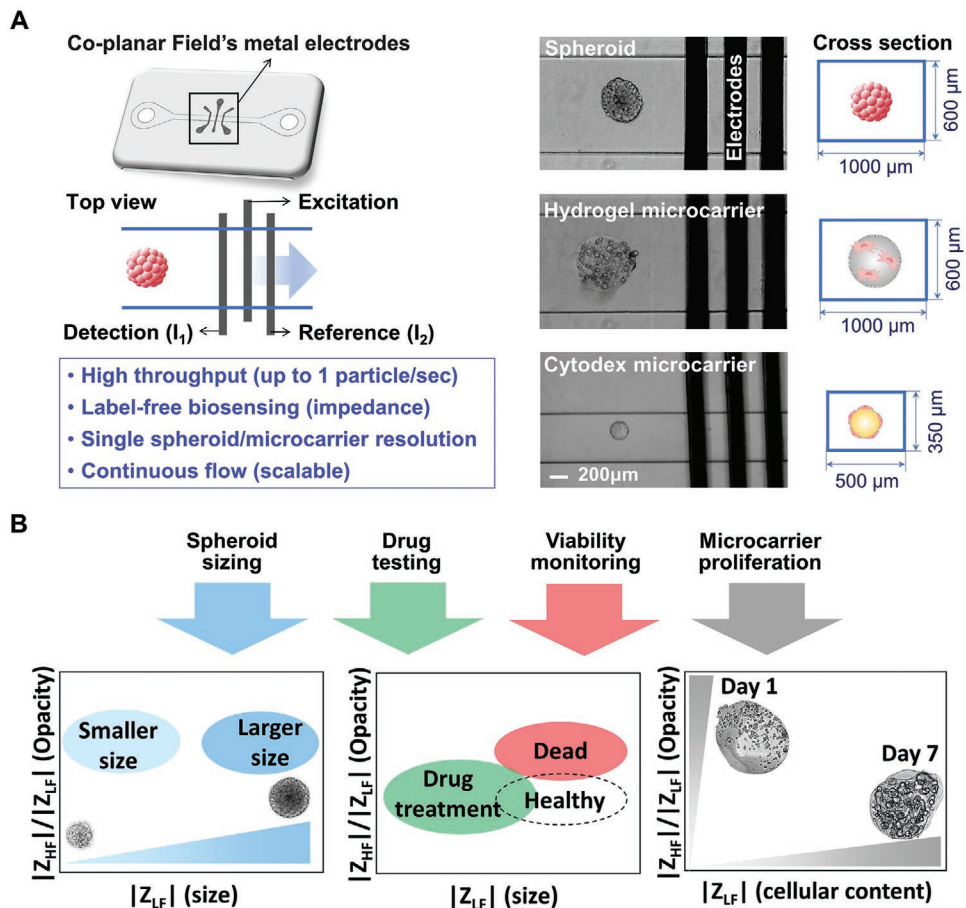


**Figure 1.** Microfluidic impedance cytometry for label-free and high throughput biosensing of 3D spheroids/microcarriers. A) Schematic illustration of device design and impedance measurement. Brightfield images of single spheroid (top), hydrogel microcarrier (middle), Cytodex 3 microcarrier (Cyto-MC) (bottom) flowing in the microchannel with co-planar Field's metal electrodes. B) Overview of device applications for spheroid monitoring (size and viability), drug assays, and microcarrier characterization.

spheroid growth in trapping cavities,<sup>[14,15]</sup> microposts array,<sup>[16]</sup> and hanging drops.<sup>[17]</sup> However, these methods have low throughput ( $\approx 1\text{--}10$  spheroids per assay)<sup>[16,17,18]</sup> and electrical characterization of such static spheroid cultures is affected by both cells and medium properties.<sup>[19]</sup> An attractive alternative is microfluidic impedance cytometry which enables continuous-flow single cell profiling based on dielectric properties (cell size, membrane, cytoplasm etc.).<sup>[20\text{--}23]</sup> To date, this technique has been widely applied for cells ( $10\text{--}30\ \mu\text{m}$ ) studies,<sup>[24\text{--}26]</sup> but not larger cell aggregates ( $>100\ \mu\text{m}$ ) due to limited understanding on cell-cell and cell-extracellular matrix dielectric properties in multi-cellular objects. Hence, developing a “scaled-up” impedance cytometer would enable continuous and label-free monitoring of larger spheroids/microcarriers to facilitate drug screening and tissue engineering research.

In this work, we report a novel low-cost microfluidic impedance cytometer for continuous-flow monitoring of 3D cultured cells by measuring single spheroid/microcarrier (Figure 1A). A soft lithography fabrication method to pattern co-planar electrodes using Field's metal (metal alloys with low melting point)<sup>[27\text{--}30]</sup> is also presented. We first performed numerical simulations to investigate the impedance of cellular aggregates, and showed that higher cell number and lower cell membrane

conductivity induced higher impedance magnitude and stronger dielectric dispersion effects (dependence of the permittivity of a dielectric material on the frequency of an applied electric field) in spheroids/hydrogel microcarriers. Next, we conducted impedance measurements of breast cancer (MCF-7) spheroids at low ( $|Z_{LF}|$ , 60 kHz) and high ( $|Z_{HF}|$ , 1 MHz) frequency to characterize spheroid biomass and viability. Increased  $|Z_{LF}|$  was observed for larger spheroids, while dead spheroids (heat-treated) exhibited higher opacities (ratio of  $|Z_{HF}| / |Z_{LF}|$ ) due to higher cell membrane permeability and electrical conductivity. We also observed low  $|Z_{LF}|$  for MCF-7 spheroids treated with anti-cancer drug (paclitaxel) as they shrunk in size due to severe cytotoxicity and cell dissociation. To demonstrate the versatility of our platform, we conducted several in vitro proof-of-concept microcarrier studies, namely, we investigated impedance changes for 1) proliferation of human skin keratinocytes (HaCaT) encapsulated in hydrogel (GelMA) microcarriers, and 2) adipose-derived mesenchymal stem cells (ADSCs) differentiation on Cytodex 3 microcarriers beads (Cyto-MCs). For both culture systems,  $|Z_{LF}|$  increased with cell content (biomass) over time. Interestingly, Cyto-MCs with differentiating ADSCs had higher opacities as compared to non-differentiating cells. Differentiated adipogenic cells (high intracellular lipid content)

also exhibited higher impedance than osteogenic cells which were calcium ions-rich (more conductive) for both microcarriers and single cell level. To the best of our knowledge, this is the first-in-kind label-free approach to monitor stem cells differentiation on microcarriers in a continuous flow. Taken together, the developed impedance biosensor offers label-free and continuous monitoring of spheroid and microcarrier cellular content at high throughput (up to 60 particles per min). We envision that this platform technology can be translated to perform large scale spheroid screening of anti-cancer drugs, as well as be integrated into bioreactors for long-term bioprocesses monitoring of biomass and cell quality (Figure 1B).

## 2. Results and Discussion

### 2.1. Numerical Simulation of Spheroids/Microcarriers

Electrical model (e.g., single shell model) for single cells is well established,<sup>[31,32]</sup> but there are limited studies for multi-cellular objects due to the high complexity in cell–cell interactions which require demanding computational resources.<sup>[33]</sup> To better understand the composite influence of individual cellular electrical properties on spheroids/microcarriers impedance, we first set up simplified 2D numerical models for spheroid and microcarrier, respectively (Figure 2A). Briefly, a spheroid/microcarrier was positioned at the center of the channel of height  $h$  and length  $w$  (refer to the Supporting Information for more details). Parameters for the simulation are listed in Table S1, Supporting Information. To study the dielectric dispersion phenomenon, special attention was paid to the current density and impedance magnitude at different frequencies. For the spheroid simulation model, cells were closely packed in a hexagon arrangement. Culture medium and cytoplasm behaved as resistors for all excitation frequencies (<100 MHz,<sup>[34]</sup>), while cell membrane acted as a capacitor due to dielectric lipid bilayer. In the low frequency regime (<10 kHz), there is less current flow through the spheroid/microcarrier (Figure 2B), thereby contributing to the high impedance. In contrast, the simulated impedance at high frequency regime decreased due to dielectric dispersion of cell membrane. This phenomenon can be explained by the fact that electric dipoles in lipid bilayer cannot follow the rapid change of oscillating electric field (high-frequency excitation),<sup>[36]</sup> allowing more current flow through the spheroid/cells. We further investigated the dependence of impedance on spheroid size and cell membrane conductivity. Figure 2C shows the effects of cell layer (i.e., spheroid size) on impedance  $|Z|$  of spheroid system at various frequencies. Increased cell layers (larger spheroid size) contributed to higher  $|Z|$  at low frequencies as the proportion of “insulator” increased while the more conductive medium volume reduced. At a higher frequency (e.g., 1 MHz), differences in  $|Z|$  resulting from different spheroid sizes became smaller as the cell membrane capacitance was “short-circuited” and the impedance magnitude was dominated by cytoplasm. As membrane disruption is a hallmark of cell death, spheroid with cell membrane of different conductivities were also simulated. As expected, higher membrane conductivity led to lower  $|Z|$  (Figure 2D) and higher opacity (ratio of  $|Z_{HF}|/|Z_{LF}|$ , Figure 2E) due to the reduced insulating effects of membrane.

For hydrogel microcarrier simulation model, single cells were placed within the hydrogel. As the conductivity of hydrogel (GelMA) was similar to culture media and much higher than cell membrane, uniform current flow through the cell-free microcarrier was observed at all frequencies (Figure 2B). Once cells were embedded in microcarrier, the capacitive behavior of cell membrane at low frequency impeded current flow. In contrast, dielectric dispersion of cell membrane at high frequency enabled current flow thereby reducing the impedance of membrane. As cells proliferate in the hydrogel microcarrier, impedance magnitude increased due to reduced portion of the more conductive culture medium in hydrogel microcarrier (Figure 2F), and opacity decreased because of the enlarged membrane area (Figure 2G).

In our 2D models, cell membrane was modeled by a contact impedance boundary condition instead of a full-fidelity thin-layer geometry.<sup>[35]</sup> This simplification reduces requirements on computational resources by circumventing the extremely fine meshing near the membrane region, and the maximum difference in their impedance magnitudes was less than 7% between both methods (Figure S1, Supporting Information). Simulated spheroid impedance also showed good agreement with experimental results with the same order of magnitude (Figure S2, Supporting Information), which further confirmed the validity of our 2D models. Both models also replicate the key physics observed experimentally including dielectric dispersion of cell membranes and spheroid size-dependent impedance magnitude. Taken together, this clearly suggests the feasibility of our 2D models to study the impedance signatures for monitoring spheroids and microcarriers.

### 2.2. Spheroid Biomass and Viability Monitoring

Cancer spheroids (tumoroids) are often studied in cancer biology to mimic cell–cell interaction and extracellular matrix in vivo.<sup>[1]</sup> While fluorescence imaging is commonly used for spheroid characterization, and it is time-consuming with limited light penetration. As electrical profiling of spheroids can potentially overcome these technical limitations,<sup>[14,16]</sup> we next studied the impedance signature of breast cancer (MCF-7) spheroids at varying excitation frequencies (Figure 3A). The impedance signal is determined by three major components: 1) impedance of electrical double layer (EDL) near the surface of electrodes that is dominant in low frequency regime (<300 kHz), 2) impedance of spheroid/microcarrier in detection region that is dominant in high frequency regime (>300 kHz), and 3) impedance of medium which remains constant. In the low frequency regime, EDL behaves as a capacitor which contributes to a relatively high impedance signal that affects spheroid impedance detection. As frequency increases, effect of EDL is minimized under the rapid alternating electric field (high frequency),<sup>[36]</sup> which is consistent with our simulation results indicating a diminishing EDL (decrease in maximum ion concentration) at higher frequencies (Figure S3, Supporting Information). In the high frequency regime, the impedance signal reduces due to dielectric dispersions ( $\beta$ -dispersion) associated with the polarization of cell membrane.<sup>[36]</sup> Experimental results also showed similar observations with low differential current responses at

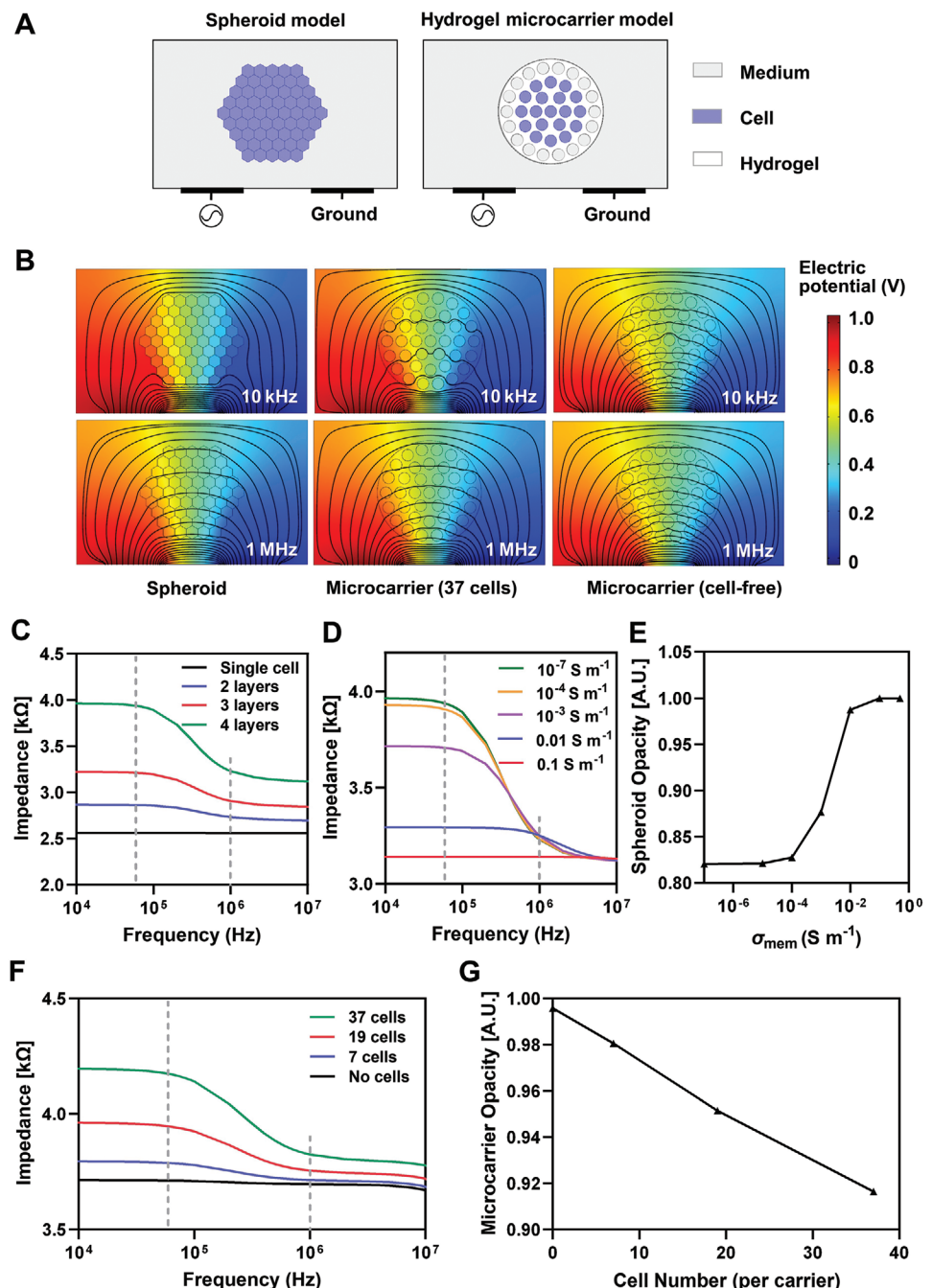


**Figure 2.** Numerical simulation results for spheroid and microcarrier. A) 2D numerical models for spheroid (left) and cell-encapsulating hydrogel microcarrier (right). Medium is represented in gray, cytoplasm in blue, and hydrogel in white. B) Electric potential distribution in spheroid and microcarrier systems at low (10 kHz) and high frequency (1 MHz). Streamlines indicate the current density ( $\text{A m}^{-2}$ ). Effects of C) spheroid size (various number of cell layers, with membrane conductivity fixed as  $10^{-7} \text{ S m}^{-1}$ ) and D) spheroid membrane conductivity (4-layer spheroid model) on impedance signal at different frequencies. E) Effect of membrane conductivity on spheroid opacity ( $|Z_{HF@1 \text{ MHz}}|/|Z_{LF@60 \text{ kHz}}|$ ). Effect of cell number (per microcarrier) on F) impedance signal and G) microcarrier opacity. Gray dash lines in graphs C, D, and F represent frequencies 60 kHz and 1 MHz.

low frequencies (indicative of EDL effect) (Figure S4A, Supporting Information). EDL effect decreased to a minimal level for both devices with 500 and 1000  $\mu\text{m}$  width channels at frequencies higher than 300 kHz (Figure S4B, Supporting Information), thus suggesting the potential of our continuous-flow impedance detection scheme.

Similar to simulation results, the impedance signal of spheroids increased with higher excitation frequencies, and decreased after reaching a peak value at 300 kHz (Figure 3A). Larger spheroids resulted in higher impedance signals for all frequencies ( $p < 0.001$  as compared to control [2k spheroid] for impedance signals at 60 kHz and 1 MHz), and the

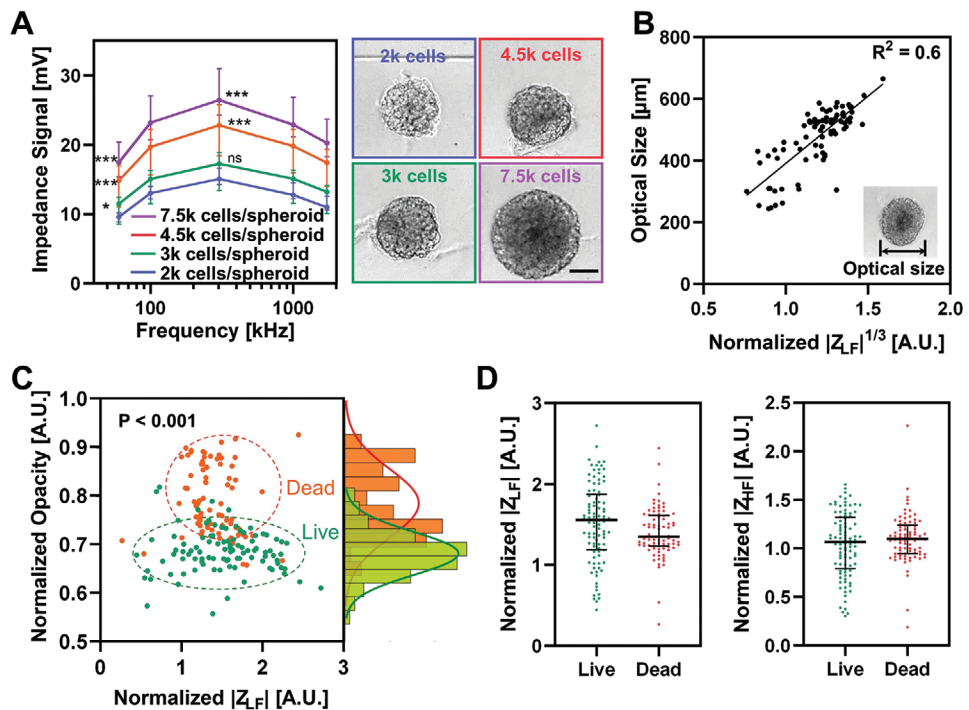


**Figure 3.** Impedance-based characterization of cancer spheroid growth and viability. A) Impedance spectroscopy analysis and brightfield images of breast cancer (MCF-7) spheroids of different sizes. \*\*\* $p < 0.001$ , \* $p < 0.05$  as compared to signals of 2k cells/spheroid. Scale bar is 200  $\mu\text{m}$ . B) Association between optical size (image based) and impedance at low frequency  $|Z_{LF}|$  (electrical based). Optical size (diameter) was plotted against  $|Z_{LF}|^{1/3}$  as  $|Z_{LF}|$  is linearly proportional to the volume of the spherical particle. C) Normalized 2D impedance scatter plot and opacity density distribution of single live and dead (heat-treated) MCF-7 spheroids. Unpaired  $t$  test yielded  $p < 0.001$  between live and dead spheroids. D) Low-frequency impedance  $|Z_{LF}|$  and high-frequency impedance  $|Z_{HF}|$  of spheroids. Error bars illustrate interquartile ranges.

low-frequency impedance  $|Z_{LF}|$  of spheroids (indicative of their electrical size) was also correlated to their optical size ( $R^2 = 0.6$ ) (Figure 3B). It should be noted that  $|Z_{LF}|$  may be affected by spheroid shape and biological heterogeneity, as well as variability of spheroid orientation during flow in the microchannel (Figure S5A, Supporting Information). Association between optical size of polystyrene beads and its  $|Z_{LF}|$  was higher ( $R^2$  of 0.89), which indicates the feasibility of characterizing spheroid size based on  $|Z_{LF}|$  (Figure S5B, Supporting Information). For spheroid viability, we used electrical opacity ( $|Z_{HF}|/|Z_{LF}|$  ratio) to characterize spheroid membrane properties and minimize the cell size dependency. Out of the six pairs of frequencies selected for  $|Z_{HF}|$  and  $|Z_{LF}|$ , live and dead spheroids were most distinguishable at 1 MHz (high) and 60 kHz (low) for spheroid viability characterization (Figure S6, Supporting Information). It should be noted that the frequency pair (1.7 MHz and 300 kHz) most commonly used for single cell characterization did not work well for spheroids possibly due to different dielectric dispersion behaviors in single cells. EDL effect was smaller in our large electrode design, and  $|Z_{LF}|$  was optimal at 60 kHz which was low enough to indicate the object size with reduced influence of EDL (Figure S4A, Supporting Information). Similar to numerical results (Figure 2E), the normalized opacities of dead spheroids (incubated at 75 °C for 1 h) were  $\approx 0.7$ –0.9, which were higher than viable spheroids ( $\approx 0.6$ –0.8, Figure 3C). This is likely attributed to the increased cell membrane permeability during cell death,<sup>[37,38]</sup> which led to higher membrane

conductivity and reduced impedance at low frequencies ( $|Z_{LF}|$ ). Membrane changes also resulted in minimal differences to impedance signals at  $|Z_{HF}|$  (Figure 3D), which was in good agreement with our simulation results (Figure 2D). Our findings showing that membrane conductivity contributed more to  $|Z_{LF}|$  than  $|Z_{HF}|$  can be explained by an equivalent circuit model. Cell membrane is modeled as a resistor (for membrane conductivity) with a capacitor (for membrane capacitance) in parallel<sup>[39]</sup> (Figure S7, Supporting Information). At low frequencies, high impedance from capacitor will impede the current flow, and the resistor (conductivity) is the main factor that determines the overall membrane impedance. At high frequencies, the impedance from capacitor becomes extremely low (short-circuited) due to the dielectric dispersion and allows more current flow, thereby minimizing the contribution from the resistor. A dead spheroid comprising of cells with compromised/leaky membrane has high overall membrane conductivity. Since it is the membrane conductivity (dominant at low frequencies) rather than capacitance that is different between live and dead spheroids, differences in impedance signals between these two groups are thus more distinguishable at low frequencies (see detailed mathematical proof in the Supporting Information). As particle size contributes to impedance at both low and high frequency, we also defined impedance ratio or opacity ( $|Z_{HF}|/|Z_{LF}|$ ) to reflect membrane properties for viability monitoring. While opacity between 0.7 and 0.8 is the overlapping region between live and dead spheroids, probability of live spheroids with

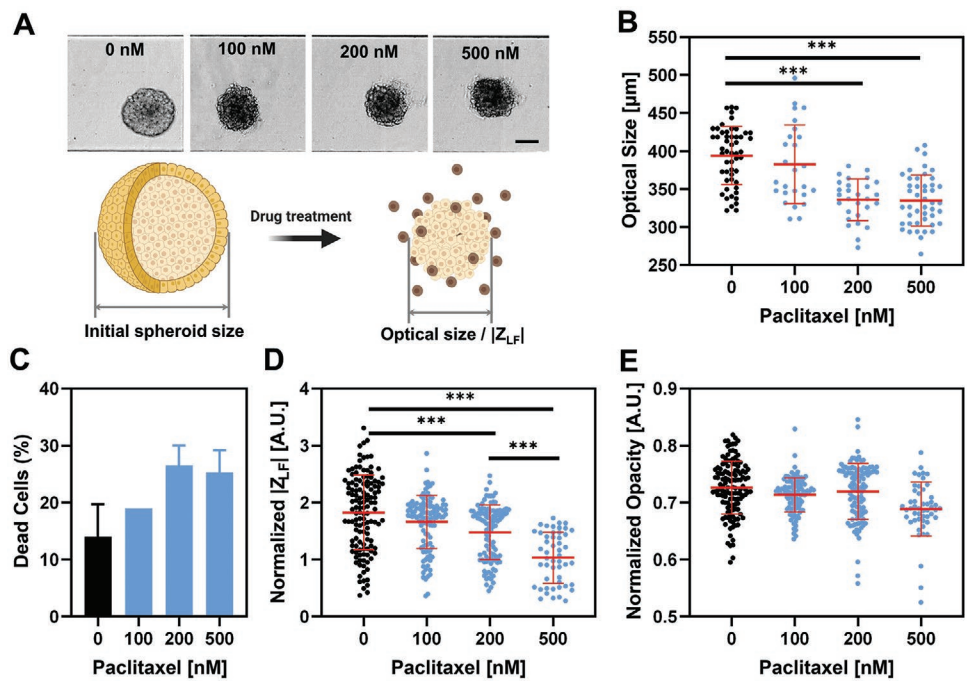


**Figure 4.** Drug susceptibility monitoring of cancer spheroids. A) Brightfield images and schematic illustration of cell dissociation from drug-treated spheroids at the outer periphery. Scale bar is 200  $\mu\text{m}$ . B) Optical sizes, C) percentage of dead cells (refer to the Supporting Information for method of viability assay), D) normalized low-frequency impedance  $|Z_{LF}|$ , and E) normalized opacity of paclitaxel (PTX)-treated spheroids at different drug concentrations. Error bars illustrate standard deviations. \*\*\* $p \leq 0.001$ .

opacity  $<0.7$  is 94.1%, and probability of dead spheroids with opacity  $>0.8$  is 94.4%, which indicates the feasibility of viability monitoring based on opacity. Taken together, these findings demonstrated the ability of impedance signature to monitor spheroid size, proliferation, and viability in a continuous-flow manner.

### 2.3. Spheroid Drug Susceptibility Monitoring

As a proof-of-concept for drug screening, we performed impedance measurements on MCF-7 spheroids treated with paclitaxel (PTX), a common anti-cancer drug for several types of cancers including ovarian cancer and breast cancer.<sup>[40,41]</sup> Optical images of drug-treated spheroids showed more disintegrated spheroid outer surface, and a decrease in spheroid size after PTX treatment for 24 h (Figure 4A,B), which was similar to a previous work reporting that PTX induced cell dissociation at the outer shell of spheroids.<sup>[42]</sup> The spheroids became smaller in size and majority of the cells in spheroids remained viable ( $\approx 25\text{--}30\%$  dead cells) after drug treatment (Figure 4C). In terms of electrical parameters, normalized  $|Z_{LF}|$  of spheroid decreased from  $1.83 \pm 0.65$  (untreated) to  $1.03 \pm 0.44$  (500 nm) in a dose-dependent manner, and were significantly different at 200 and 500 nm PTX concentrations ( $p < 0.001$ ) (Figure 4D). We observed negligible changes in the opacities of the drug-treated spheroids (Figure 4E) as majority of the cells remained viable (Figure 4C) or were in the process of undergoing apoptosis. These findings clearly indicate that drug screening assays can be performed based on spheroid native impedance signatures

( $|Z_{LF}|$ ), which obviates the need for laborious and expensive fluorescent staining. To ensure that the assay results were not affected by experimental setup, we performed repeated measurements ( $>10$  times) of same spheroids (non-drug treated) in a closed recirculation. Although change in spheroid orientation (during flow) may affect the signal, the average deviations for  $|Z_{LF}|$  and opacity were only 12.73% and 3.53%, respectively (Figure S8, Supporting Information). This result indicates a high detection consistency and gentle nature of our flow-based sensing approach for label-free and continuous spheroid sampling.

### 2.4. Impedance-Based Monitoring of Cells Encapsulated in Microcarriers

Cell-encapsulated hydrogel microcarriers are widely used in tissue engineering and 3D cell culture,<sup>[43]</sup> but it is non-trivial to track the biomass using imaging, and enzymatic methods for single cell characterization are generally ineffective for encapsulated cells.<sup>[44]</sup> We next studied the capabilities of the developed platform for monitoring human skin keratinocytes (HaCaT) encapsulated within hydrogel (GelMA) microcarriers. As HaCaT cells proliferated (doubling time of  $\approx 24$  h in 2D culture<sup>[45]</sup>) in hydrogel microcarriers, the microcarriers remained similar in size (Figure 5A). Since hydrogel is more conductive than cells, the increased cell numbers in hydrogel microcarrier during cell proliferation will cause an increase in impedance ( $|Z_{LF}|$ ), and thus a lower opacity (Table S2, Supporting Information). Hence, the opacity of microcarriers decreased over

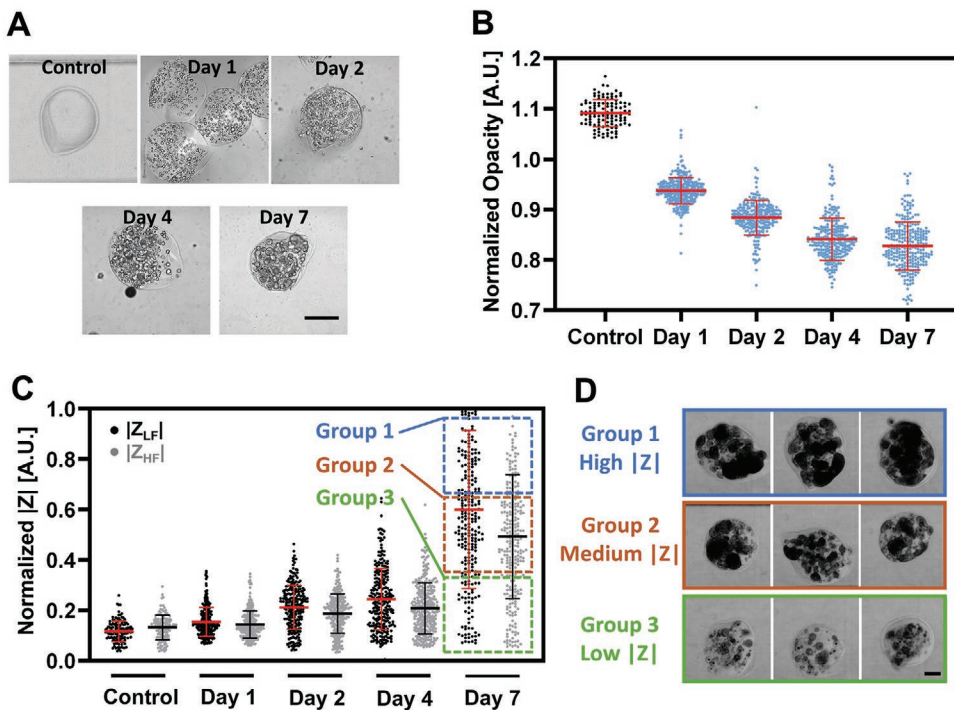


**Figure 5.** Impedance-based characterization of keratinocytes (HaCaT) encapsulated in GelMA hydrogel microcarriers. A) Optical images of empty and cell-containing hydrogel microcarriers over time. Scale bar is 300  $\mu\text{m}$ . B) Normalized opacity, and C) normalized impedance signals at low (60 kHz, black) and high (1 MHz, gray) frequency of hydrogel microcarriers over time. Error bars represent standard deviation. Data points at day 7 were divided into 3 groups (colored boxes) based on their  $|Z|$  magnitudes. D) Representative brightfield images of hydrogel microcarriers with high  $|Z|$  (group 1), medium  $|Z|$  (group 2) and low  $|Z|$  (group 3) signals on day 7. Scale bar is 300  $\mu\text{m}$ .

time (Figure 5B), which was consistent with the simulation results (Figure 2G). In 3D cell culture, higher cell numbers would reduce the physical space filled with culture medium, which led to increased microcarrier impedance. The opacity became more divergent as hydrogel and cells exhibited different extent of dielectric dispersion, and the microcarriers would change from an initial hydrogel-dominated state (low dispersion) to a cell-dominated state (greater dielectric dispersion) after culture. Hence, the impedance signals of  $|Z_{LF}|$  and  $|Z_{HF}|$  became increasingly different over time (Figure 5C), which is consistent with the simulation results that higher biomass in microcarrier induced larger magnitude change in  $|Z_{LF}|$  as compared to  $|Z_{HF}|$  (Figure 2F). It is noted that the distribution of electrical profiles ( $|Z|$  and opacity) became more heterogeneous over time. This is attributed to differences in cell densities encapsulated in hydrogel microcarriers during fabrication (initial stage) that became apparent after several days of culture. Another possible reason is the formation of cell aggregates (typical phenotype of epithelial cells in suspension) within the microcarrier at higher cell densities as shown in the representative optical images of microcarriers with high (group 1), medium (group 2), and low (group 3) impedance magnitudes (Figure 5D). The cell aggregates affected membrane surface area, which may contribute to the higher impedance signals as observed in group 1. Taken together, these results indicate the potential of the developed platform for label-free monitoring of biomass status in cell-encapsulated microcarrier culture.

## 2.5. Impedance-Based Monitoring of Stem Cell Differentiation on Cytodex Microcarriers

Stem cells are widely used in regenerative medicine,<sup>[46]</sup> but they tend to lose their pluripotency after multiple passages.<sup>[47]</sup> As microcarriers have high surface area-to-volume ratio, they are widely used in bioreactors to provide sufficient sample materials for cell therapies.<sup>[48]</sup> However, characterization of stem cells on microcarriers rely on immunofluorescence or enzymic detachment for single cell endpoint analysis.<sup>[7]</sup> To determine if impedance-based monitoring can be applied for stem cells attached on microcarriers, we performed experiments to characterize ADSCs proliferation and differentiation on commercial collagen-coated dextran microcarriers (Cytodex 3) (Cyto-MCs) (Figure 6A). Impedance measurement of Cyto-MCs seeded with ADSCs was conducted daily (Day 0 to 3) to monitor the cell proliferation, and every 3 or 4 days to characterize ADSCs differentiation into adipogenic and osteogenic lineages (Day 0 to 13). Similar to hydrogel microcarriers, the impedance magnitude of cell-attached Cyto-MCs increased over time due to the increasing biomass and cell coverage area on Cyto-MCs surfaces (Figure 6B).

When ADSCs reached 60%–80% confluence on Cyto-MCs, differentiation process was initiated as previously described.<sup>[49–51]</sup> As shown in the nucleus-stained (DAPI) images of Cyto-MCs (Figure 6C), cell proliferated slower during differentiation as cell densities on Cyto-MCs cultured in DMEM were higher than in adipogenic medium (AM) and osteogenic medium (OM). By Day 6, some non-differentiated cells in

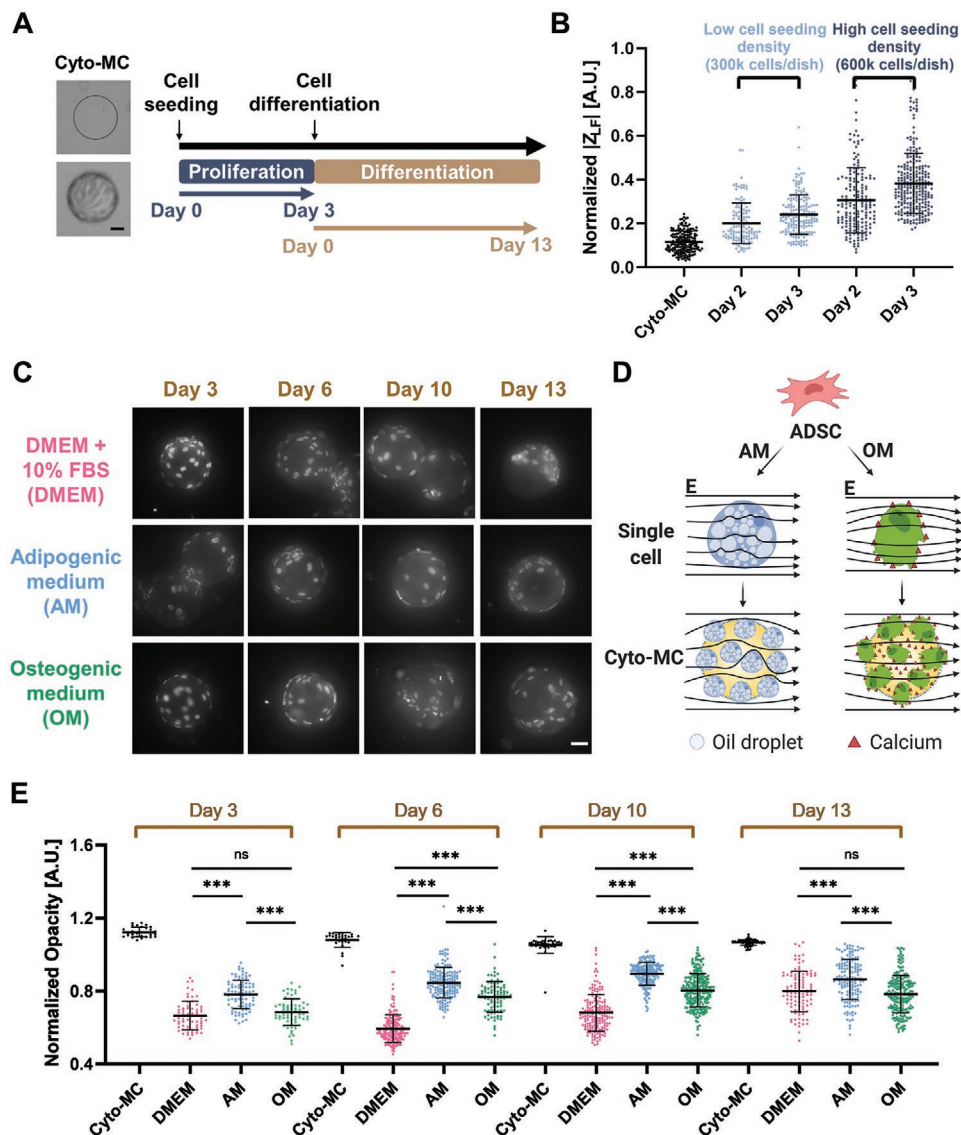


**Figure 6.** Impedance-based characterization of stem cell differentiation on Cytodex microcarriers (Cyto-MCs). A) Brightfield images of Cyto-MCs with and without adipose-derived mesenchymal stem cells (ADSCs). Timeline of stem cell culture and differentiation processes. Scale bar is 50  $\mu\text{m}$ . B) Normalized  $|Z_{LF}|$  of Cyto-MCs seeded with different cell densities. C) Fluorescent images (DAPI-stained) of cells on Cyto-MCs cultured in DMEM with 10% FBS (DMEM) as control, adipogenic medium (AM) for adipogenic differentiation, and osteogenic medium (OM) for osteogenic differentiation. Scale bar is 50  $\mu\text{m}$ . D) Proposed schematic illustration of cellular dielectric properties of differentiated ADSCs for adipocytes (blue) and osteocytes (green) as single cells and on Cyto-MCs. Black lines represent the electric field (E). E) Normalized opacity of Cyto-MCs with differentiating ADSCs on different days.

DMEM began to detach due to over confluence. In terms of cell impedance, we hypothesize that differentiated adipogenic cells (AM) contain non-conductive lipid droplets which will impede the electric field (higher impedance), while osteogenic cells (OM) are more conductive with more calcium ions in cell membrane (lower impedance) and secreted onto the Cyto-MCs (Figure 6D).<sup>[52]</sup> Figure 6E shows the opacity ( $|Z_{HF}|/|Z_{LF}|$ ) distribution of Cyto-MCs with differentiating and undifferentiating cells. For all timepoints, it was observed that Cyto-MCs cultured in DMEM had the lowest opacity, Cyto-MCs in AM yielded highest opacity, and Cyto-MCs in OM had opacity between DMEM and AM. These differences in Cyto-MCs

opacity might be related to two factors namely, 1) cell number on Cyto-MCs (i.e., cell coverage ratio), and 2) impedance differences between single differentiated adipogenic cells and osteogenic cells. Due to slower cell proliferation during differentiation, Cyto-MCs cultured in AM and OM had significantly higher opacities than DMEM ( $p < 0.001$ ) with lower cell numbers (lower  $|Z_{LF}|$ ). As Cyto-MCs opacities of AM were consistently higher than OM ( $p < 0.001$ ), we further performed single cell impedance analysis of differentiated ADSCs using a different microscale impedance-based cytometer.<sup>[53,54]</sup> Interestingly, the non-conductive lipid droplets (Oil Red O staining in Figure S9A, Supporting Information) in differentiating

adipogenic cells indeed contributed to higher impedance signals for both  $|Z|_{300\text{ kHz}}$  and  $|Z|_{1.7\text{ MHz}}$ , and thus higher opacity at single cell level (Figure S9B, Supporting Information). In contrast, osteogenic differentiating cells had lower impedance values, which indicated they were more conductive with increased membrane calcium ions (Alizarin Red S staining in Figure S9A, Supporting Information). Adipogenic cells were also slightly larger in size which could lead to higher impedance for both single cells and on Cyto-MCs (Figure S9C,D, Supporting Information). Taken together, these intriguing results clearly indicate the potential of direct impedance-based monitoring of stem cell proliferation and differentiation in microcarrier-based bioreactors.

### 3. Conclusions

In summary, we have developed a novel “scaled-up” and low-cost microfluidic impedance cytometer using Field’s metal for label-free and non-invasive monitoring of 3D cell culture (e.g., spheroids and microcarriers) under continuous flow. Micro-channel and electrodes geometries, and impedance detection frequencies were optimized to ensure single spheroid/microcarrier detection with high sensitivity. We demonstrated that the closed-loop recirculation system is capable of tracking 1) spheroid culture (size, viability, and drug susceptibility), and 2) cell-encapsulated hydrogel and cell-attached Cytodex microcarriers by quantifying multi-dimensional impedance signals. Remarkably, stem cell differentiation on microcarriers can be monitored directly based on impedance profile due to inherent electrical differences of single adipogenic (lipid-rich, high impedance) and osteogenic (calcium ions, more conductive) cells. Taken together, the developed impedance biosensor offers great versatility for multi-parametric analysis of 3D spheroids/microcarriers at high throughput ( $\approx 1$  particle per second), and can be readily integrated into bioreactors for long-term and remote bioprocess monitoring of biomass and cell quality.

### 4. Experimental Section

**Numerical Simulation:** 2D numerical simulation of spheroid/microcarrier on coplanar electrodes was setup using the Electric Currents (ec) module in COMSOL Multiphysics 5.0. The electrical double layer (EDL) which forms naturally near the electrode surface would not affect the study of impedance response induced by changed spheroid/microcarrier properties (e.g., spheroid size, cell membrane conductivity, etc.). Therefore, EDL near the surface of electrodes was excluded in this model for simplicity. In the 2D model, a spheroid/microcarrier was located at the center of the channel of height  $h$  and length  $w$  (Figure 2A). The channel was filled with medium of electrical conductivity  $\sigma_m$  and relative permittivity  $\epsilon_m$ . Spheroid/microcarrier contained cells of diameter  $d_{\text{cell}}$  with membrane resistance  $\rho_{\text{mem}}$  (obtained based on membrane conductivity  $\sigma_{\text{mem}}$ ) and capacitance  $C_{\text{mem}}$ . The permittivity and conductivity of cytoplasm were  $\epsilon_{\text{cyto}}$ , and  $\sigma_{\text{cyto}}$ , respectively. Inside the spheroid, cells were in a hexagon arrangement, which mimicked the circular shape of spheroid. To simulate spheroids of different sizes, cells were added to the outmost layer. The cell-encapsulating porous hydrogel microcarrier (permittivity  $\epsilon_{\text{gel}}$  and conductivity  $\sigma_{\text{gel}}$ ) was designed with pre-defined porosity (vacant sites (circles) for medium and cells). To mimic cell proliferation within the microcarrier over time, cells (blue circle) occupied more and more vacant sites that initially filled with

medium (gray circle). To simulate electrical measurement, alternating voltage of different frequencies was applied to the left electrode, while keeping the right electrode grounded. The electric potential distribution was governed by ohmic conduction:

$$\nabla \cdot \mathbf{J} = Q \quad (1)$$

$$\mathbf{J} = \sigma \mathbf{E} + j\omega \mathbf{D} + \mathbf{J}_e \quad (2)$$

$$\mathbf{E} = \nabla \cdot \mathbf{V} \quad (3)$$

where  $\mathbf{J} \equiv \mathbf{J}(x,y,t)$  was the current density ( $\text{A m}^{-2}$ ),  $\mathbf{E} \equiv \mathbf{E}(x,y,t)$  was the electric field ( $\text{V m}^{-1}$ ),  $\mathbf{D} \equiv \mathbf{D}(x,y,t)$  was the electric displacement field ( $\text{C m}^{-2}$ ),  $\mathbf{J}_e \equiv \mathbf{J}_e(x,y,t)$  was the external current density ( $\text{A m}^{-2}$ ), and  $\mathbf{V} \equiv \mathbf{V}(x,y,t)$  was the electric potential (V). Electric insulation boundary condition was applied to the boundaries of the system, except for the part where external voltage was applied.

$$\mathbf{n} \cdot \mathbf{J} = 0 \quad (4)$$

where  $\mathbf{n}$  was the normal vector perpendicular to the boundary pointing out of the computational domain.

Alternating voltage of magnitude of  $V_L$  was applied to the left electrode.

$$V = V_L \quad (5)$$

The right electrode was grounded.

$$V = V_R = 0 \quad (6)$$

Contact impedance condition is applied to cell boundaries to mimic the cell membrane.

$$\mathbf{n} \cdot \mathbf{J}_1 = \left( \frac{1}{\rho_{\text{mem}}} + j\omega C_{\text{mem}} \right) (V_1 - V_2) \quad (7)$$

$$\mathbf{n} \cdot \mathbf{J}_2 = \left( \frac{1}{\rho_{\text{mem}}} + j\omega C_{\text{mem}} \right) (V_2 - V_1) \quad (8)$$

where  $\mathbf{J}_1$  was the current density from the region outside of membrane to the inside of membrane, and  $\mathbf{J}_2$  was the current density in opposite direction of  $\mathbf{J}_1$ .  $V_1$  and  $V_2$  are electric potential at regions outside and inside of membrane, respectively.

The governing equations 1, 2, and 3 were solved with the boundary conditions 4–6 using finite element methods in frequency domain. The current was obtained by integrating the current density along the central line of the model (see Figure S10, Supporting Information), after which impedance was obtained by  $|Z| = V_{\text{rms}}/I_{\text{rms}}$ . Impedance responses to different cell number (spheroid size) and cell membrane conductivity  $\sigma_{\text{mem}}$  (reflecting viability) at different frequencies were analyzed and compared with experimental results.

**Device Design and Fabrication:** Polydimethylsiloxane (PDMS, Dow Corning) based microfluidic devices were fabricated using standard soft lithography techniques.<sup>[55]</sup> The device consisted of two PDMS layers namely electrode layer (bottom), and microchannel layer (top) (Figure S11, Supporting Information). For the electrode layer channel design, three one inlet-one outlet microchannels of width 200  $\mu\text{m}$  were separated by gaps of 200  $\mu\text{m}$  in parallel. The “200  $\mu\text{m}$  (electrode) + 200  $\mu\text{m}$  (gap) + 200  $\mu\text{m}$  (electrode)” configuration approximated to a single spheroid size, which can largely minimize the probability of two or more spheroids/microcarriers being detected simultaneously. In addition, the 200  $\mu\text{m}$  gap was wide enough for robust Field’s metal manual loading, and to ensure the differential signal collected from two side electrodes (one for signal detection and the other as reference signal) were distinguishable with minimal environmental noise. For the microchannel layer design, the one inlet-one outlet main channel of

1 mm width and 600  $\mu\text{m}$  height was used to allow perfusion of spheroids and hydrogel microcarrier ( $\approx 500$  to  $600 \mu\text{m}$ ) whereas a smaller channel of 500  $\mu\text{m}$  width and 300  $\mu\text{m}$  height was used for Cyto-MCs ( $\approx 175 \mu\text{m}$ ). To pattern electrodes for impedance measurement, the electrode layer was first pressed against aluminium foil. Field's metal (EGain) was loaded into the inlet by heating the chip on a hot plate at 100 °C. After cooling to room temperature and peeling off the aluminium foil, the electrodes layer and main channel layer were bonded by air plasma treatment (Harrick Plasma). Finally, wires were connected to the electrodes using localized heating at the inlet by hot air gun to prevent damaging the solidified electrodes (Figure S11, Supporting Information).

**Stem Cell Differentiation on Cyto-MCs:** Cyto-MCs with ADSCs were cultured in Dulbecco's Modified Eagle's Medium (DMEM, Gibco) supplemented with 10% Fetal Bovine Serum (FBS, Gibco) and 1% penicillin/streptomycin (P/S, Gibco) in petri dishes. Differentiation was initiated when ADSCs reached 60%–80% confluence on Cyto-MCs by replacing the culture medium with adipogenic medium and osteogenic medium. The adipogenic medium consisted of DMEM high glucose (Sigma) supplemented with 10% FBS, 1% P/S, dexamethasone (1  $\mu\text{M}$ , Sigma), isobutylmethylxanthine (IBMX, 0.5 mM, Sigma), and indomethacin (50  $\mu\text{M}$ , Sigma). The osteogenic medium consisted of DMEM high glucose supplemented with 10% FBS, 1% P/S, 100 nM dexamethasone, 10 mM sodium  $\beta$ -glycero phosphate (Sigma), and ascorbic acid (0.05 mM, Sigma). For undifferentiated control, Cyto-MCs with ADSCs were cultured in DMEM supplemented with 10% FBS and 1% P/S. Cells were maintained in humidified incubator at 37 °C and 5% CO<sub>2</sub> for a 13-day period with medium changed every 3 or 4 days.

**Microfluidic Operation and Signal Processing:** Prior experiments, the device and tubings were primed with 1  $\times$  PBS containing 0.5% bovine serum albumin (BSA, Miltenyi Biotec) to prevent spheroid/particle adhesion. A peristaltic pump (L100-1S-2, Longer) was used to recirculate spheroids/microcarriers ( $\approx 10$  spheroids per mL and  $\approx 60$  microcarriers per mL) at a volumetric flow rate of 1 mL min<sup>-1</sup>. To establish electrical measurement using lock-in amplifier (HF2LI, Zurich instruments), alternating excitation of different frequencies was applied to the center electrode (excitation electrode) whereas differential current response was measured from two side electrodes (the left: detection electrode, and the right: reference electrode) and converted to impedance signal (voltage) using transimpedance amplifiers (DHPCA-100, FEMTO). As a spheroid or microcarrier flows through the detection region, multifrequency impedance signals ( $I_1$ – $I_2$ , where  $I_1$  was the electrical current at the detection electrode, and  $I_2$  was the current at the reference electrode) were measured at a sampling rate of 7.2 kHz and single processing provides two electrical parameters to represent each spheroid/microcarrier: 1) impedance magnitude at low frequency ( $|Z_{LF}|$ , at 60 kHz) to determine spheroid size and microcarrier proliferation status; 2) opacity (ratio of impedance at high frequency ( $|Z_{HF}|$ , at 1 MHz) to impedance at low frequency ( $|Z_{LF}|$ , at 60 kHz)) to determine cellular activities/content of spheroids/microcarriers. Opacity was normalized to opacity of polystyrene beads (150 and 250  $\mu\text{m}$  beads for 500  $\mu\text{m}$  and 1 mm width channel respectively) as internal control.

## Supporting Information

Supporting Information is available from the Wiley Online Library or from the author.

## Acknowledgements

This research was supported by the Singapore Ministry of Education Academic Research Fund Tier 1 (RG53/18) and A. Menarini Biomarkers Pte Ltd. L.G. acknowledges support for the NTU PhD Research Scholarship. C.P. acknowledges support for the NTU-RSB Postdoctoral Fellowship. Schematics were created with BioRender.com.

## Conflict of Interest

The authors declare no conflict of interest.

## Author Contributions

C.P., L.G., C.Y.T., and H.W.H. designed the research. L.G. and C.P. performed the device fabrication and spheroid experiments. L.G., P.L.T., and L.P.T. performed the hydrogel microcarrier experiments. L.G. and P.S. performed the stem cell experiments. L.G. performed the numerical simulations. L.G., C.P., and H.W.H. analyzed the data. L.G., C.P., and H.W.H. wrote the manuscript. All authors reviewed the manuscript.

## Data Availability Statement

Research data are not shared.

## Keywords

biomanufacturing, impedance cytometry, label-free, microfluidics, stem cell differentiation

Received: November 27, 2020

Revised: February 11, 2021

Published online: March 24, 2021

- [1] F. Hirschhaeuser, H. Menne, C. Dittfeld, J. West, W. Mueller-Klieser, L. A. Kunz-Schughart, *J. Biotechnol.* **2010**, *148*, 3.
- [2] L. A. Kunz-Schughart, J. P. Freyer, F. Hofstaedter, R. Ebner, *J. Biomol. Screening* **2004**, *9*, 273.
- [3] M. Vinci, S. Gowan, F. Boxall, L. Patterson, M. Zimmermann, W. Court, C. Lomas, M. Mendiola, D. Hardisson, S. A. Eccles, *BMC Biol.* **2012**, *10*, 29.
- [4] X. Zhao, Q. Lang, L. Yildirim, Z. Y. Lin, W. Cui, N. Annabi, K. W. Ng, M. R. Dokmeci, A. M. Ghaemmaghami, A. Khademhosseini, *Adv. Healthcare Mater.* **2016**, *5*, 108.
- [5] B. Li, X. Wang, Y. Wang, W. Gou, X. Yuan, J. Peng, Q. Guo, S. Lu, *J. Orthopaedic Transl.* **2015**, *3*, 51.
- [6] T. K.-P. Goh, Z.-Y. Zhang, A. K.-L. Chen, S. Reuveny, M. Choolani, J. K. Y. Chan, S. K.-W. Oh, *BioRes. Open Access* **2013**, *2*, 84.
- [7] C. Y. M. Hsu, T. Walsh, B. S. Borys, M. S. Kallos, D. E. Rancourt, *Mol. Ther.–Methods Clin. Dev.* **2018**, *9*, 376.
- [8] S. Frauenschuh, E. Reichmann, Y. Ibold, P. M. Goetz, M. Sitterer, J. Ringe, *Biotechnol. Prog.* **2007**, *23*, 187.
- [9] J. Kieninger, A. Weltin, H. Flamm, G. A. Urban, *Lab Chip* **2018**, *18*, 1274.
- [10] G. Mehta, A. Y. Hsiao, M. Ingram, G. D. Luker, S. Takayama, *J. Controlled Release* **2012**, *164*, 192.
- [11] S. Raghavan, P. Mehta, E. N. Horst, M. R. Ward, K. R. Rowley, G. Mehta, *Oncotarget* **2016**, *7*, 16948.
- [12] Z. Wu, H. K. Lim, S. J. Tan, A. Gautam, H. W. Hou, K. W. Ng, N. S. Tan, C. Y. Tay, *Small* **2020**, *16*, 2003757.
- [13] M. Grossi, B. Riccò, *J. Sens. Sens. Syst.* **2017**, *6*, 303.
- [14] Y. Pan, D. Jiang, C. Gu, Y. Qiu, H. Wan, P. Wang, *Microsyst. Nanoeng.* **2020**, *6*, 23.
- [15] D. Kloss, M. Fischer, A. Rothermel, J. C. Simon, A. A. Robitzki, *Lab Chip* **2008**, *8*, 879.
- [16] K. Luongo, A. Holton, A. Kaushik, P. Spence, B. Ng, R. Deschenes, S. Sundaram, S. Bhansali, *Biomicrofluidics* **2013**, *7*, 034108.

- [17] Y. R. F. Schmid, S. C. Bürgel, P. M. Misun, A. Hierlemann, O. Frey, *ACS Sens.* **2016**, 1, 1028.
- [18] C. Hildebrandt, H. Butth, S. Cho, H. Impidjati, Thielecke, *J. Biotechnol.* **2010**, 148, 83.
- [19] Q. Wu, X. Wei, Y. Pan, Y. Zou, N. Hu, P. Wang, *Biomed. Microdevices* **2018**, 20, 82.
- [20] T. Sun, H. Morgan, *Microfluid. Nanofluid.* **2010**, 8, 423.
- [21] K. C. Cheung, M. Di Berardino, G. Schade-Kampmann, M. Hebeisen, A. Pierzchalski, J. Bocsi, A. Mittag, A. Tárnok, *Cytometry, Part A* **2010**, 77, 648.
- [22] J. Chen, C. Xue, Y. Zhao, D. Chen, M.-H. Wu, J. Wang, *Int. J. Mol. Sci.* **2015**, 16, 9804.
- [23] C. Petchakup, K. Li, H. Hou, *Micromachines* **2017**, 8, 87.
- [24] C. Bernabini, D. Holmes, H. Morgan, *Lab Chip* **2011**, 11, 407.
- [25] A. De Ninno, R. Reale, A. Giovinazzo, F. R. Bertani, L. Businaro, P. Bisegna, C. Matteucci, F. Caselli, *Biosens. Bioelectron.* **2020**, 150, 111887.
- [26] D. Yang, Y. Ai, *Lab Chip* **2019**, 19, 3609.
- [27] J. Panwar, R. Roy, bioRxiv:278069 **2019**.
- [28] D. Yang, Y. Zhou, Y. Zhou, J. Han, Y. Ai, *Biosens. Bioelectron.* **2019**, 133, 16.
- [29] J. Panwar, R. Roy, *Microelectron. Eng.* **2019**, 215, 111010.
- [30] T. V. Neumann, M. D. Dickey, *Adv. Mater. Technol.* **2020**, 5, 2000070.
- [31] T. Sun, S. Gawad, N. G. Green, H. Morgan, *J. Phys. D: Appl. Phys.* **2006**, 40, 1.
- [32] H. Morgan, T. Sun, D. Holmes, S. Gawad, N. G. Green, *J. Phys. D: Appl. Phys.* **2006**, 40, 61.
- [33] K. Asami, K. Sekine, *J. Phys. D: Appl. Phys.* **2007**, 40, 2197.
- [34] P. Mehrotra, B. Chatterjee, S. Sen, *Sensors* **2019**, 19, 1013.
- [35] COMSOLAB, Contact Impedance Comparison.pdf, [https://www.comsol.com/model/download/735471/models.acdc.contact\\_impedance\\_comparison.pdf](https://www.comsol.com/model/download/735471/models.acdc.contact_impedance_comparison.pdf) (accessed: February 2021).
- [36] V. Raicu, Y. Feldman, *Dielectric Relaxation in Biological Systems: Physical Principles, Methods, and Applications*, Oxford University Press, Oxford **2015**.
- [37] A. Ebrahimi, L. N. Csonka, M. A. Alarm, *Biophys. J.* **2018**, 114, 609.
- [38] A. Blicher, K. Wodzinska, M. Fidorra, M. Winterhalter, T. Heimburg, *Biophys. J.* **2009**, 96, 4581.
- [39] K. Cheung, S. Gawad, P. Renaud, *Cytometry, Part A* **2005**, 65A, 124.
- [40] E. A. Perez, *Oncologist* **1998**, 3, 373.
- [41] L. M. Zasadil, K. A. Andersen, D. Yeum, G. B. Rocque, L. G. Wilke, A. J. Tevaarwerk, R. T. Raines, M. E. Burkard, B. A. Weaver, *Sci. Transl. Med.* **2014**, 6, 229ra43.
- [42] O. Kutuk, A. Letai, *Cell Death Differ.* **2010**, 17, 1624.
- [43] A. B. Bello, D. Kim, D. Kim, H. Park, S. H. Lee, *Tissue Eng., Part B* **2020**, 26, 164.
- [44] B. A. Aguado, W. Mulyasasmita, J. Su, K. J. Lampe, S. C. Heilshorn, *Tissue Eng., Part A* **2011**, 18, 806.
- [45] V. G. Wilson, in *Epidermal Cells*, Springer, New York **2013**, pp. 33–41.
- [46] B. Lukomska, L. Stanaszek, E. Zuba-Surma, P. Legosz, S. Sarzynska, K. Drela, *Stem Cells Int.* **2019**, 2019, 9628536.
- [47] C. Allegrucci, L. E. Young, *Hum. Reprod. Update* **2006**, 13, 103.
- [48] C. J. Hewitt, K. Lee, A. W. Nienow, R. J. Thomas, M. Smith, C. R. Thomas, *Biotechnol. Lett.* **2011**, 33, 2325.
- [49] H. Yang, K. T. Nguyen, D. T. Leong, N. S. Tan, C. Y. Tay, *ACS Appl. Mater. Interfaces* **2016**, 8, 26591.
- [50] H. Yang, N. M. J. Cheam, H. Cao, M. K. H. Lee, S. K. Sze, N. S. Tan, C. Y. Tay, *Adv. Healthcare Mater.* **2019**, 8, 1900929.
- [51] P. Shi, Y. Wan, A. Grandjean, J.-M. Lee, C. Y. Tay, *Chemosphere* **2021**, 269, 128719.
- [52] R. C. Nordberg, J. Zhang, E. H. Griffith, M. W. Frank, B. Starly, E. G. Lobo, *Stem Cells Transl. Med.* **2017**, 6, 502.
- [53] C. Petchakup, H. M. Tay, W. H. Yeap, R. Dalan, S. C. Wong, K. H. Li, H. W. Hou, *Biosens. Bioelectron.* **2018**, 118, 195.
- [54] C. Petchakup, H. M. Tay, K. H. Li, H. W. Hou, *Lab Chip* **2019**, 19, 1736.
- [55] H. M. Tay, S. Kharel, R. Dalan, Z. J. Chen, K. K. Tan, B. O. Boehm, S. C. J. Loo, H. W. Hou, *NPG Asia Mater.* **2017**, 9, e434.